High-Order Semi-Implicit Simulation of Hypersonic Boundary Layer Stability and Transition

Haibo Dong *and Xiaolin Zhong †

University of California, Los Angeles, California 90095

Abstract

This paper presents and evaluates a semi-implicit method for efficient and high-order accurate computations for the stability and transition of hypersonic boundary layers. For this problem, if explicit schemes are used to advance the equations in time, the small grid sizes in wall-normal direction in the boundary layers imposed severe restriction on time steps. But global implicit methods are seldom used because they will take a prohibitively large amount of CPU time and large memory to convert full implicit equations. In the current method, the spatial discretization of the governing equations is separated into stiff terms involving derivatives along the wall-normal direction and nonstiff terms of the rest. The split equations are then advanced in time using second or third-order semi-implicit schemes so that implicit methods are used to treat the stiff terms while more efficient explicit methods can still be used for the nonstiff terms. The strict limitation on time steps due to fine grids in the wall-normal direction is removed by semi-implicit method so that the time steps only depend on the grid spacing in the streamwise direction and accuracy requirement. The efficiency and accuracy of the new semi-implicit algorithm have been tested in computing the unsteady Navier-Stokes equations for several cases.

Introduction

The prediction of laminar-turbulent transition of hypersonic boundary layers is critical to the accurate calculations of drag and thermal loads for the aerodynamic design and control of hypersonic space vehicles [1]. In recent years, direct numerical simulation has become a powerful tool in the study of fundamental flow physics of the stability and transition of boundary layers. The DNS of compressible boundary layer transition has been carried out by several research groups [2-12]. These studies show that the DNS of high-speed boundary layer transition is feasible on existing computers using efficient and accurate numerical methods. All these simulations are explicit methods, assuming a simple flat

*Graduate Student, haibo@seas.ucla.edu

†Associate Professor, Mechanical and Aerospace Engineering Department, Member AIAA.

surface without the presence of shock waves. Explicit high-order finite-difference methods are used in the non-periodic streamwise and wall-normal directions, and the Fourier spectral collocation methods are used in the periodic spanwise direction [9,12,13]. But it is difficult to apply existing numerical methods for compressible boundary layer DNS to hypersonic boundary layers over blunt bodies, due to the lack of efficient semi-implicit numerical methods for compressible viscous flows [14], difficulty in computing transient hypersonic flow with shock waves, and the stiffness of the equations in reacting hypersonic flows.

The difficulty in using explicit methods for DNS of hypersonic flow is that the Navier-Stokes equations are stiff for explicit numerical schemes. For unsteady viscous flow calculations, the extremely small grid sizes in the boundary layers near the wall is used. The stiffness of the governing equations refers to the fact that the time steps required by the stability requirement in the calculations are much smaller than that needed by accuracy consideration so that it is difficult to perform the simulation in reasonable computation times. This requires implicit treatment in numerical computations. But it is computationally expensive to do full implicit iterative calculations at every time step of the transient flow computations. In addition, because of the accuracy requirement in computing the development of transient instability waves in the streamwise direction, the computations in the streamwise direction are explicit. Therefore, a compromise between computational efficiency and numerical accuracy for the DNS studies is the semi-implicit methods, where only the derivatives in the wall-normal direction are treated implicitly.

[15,16] have started the work on developing a new set of semi-implicit Runge-Kutta schemes of for the robust and accurate temporal discretization of stiff equations for the DNS of hypersonic flows. Three kinds of time-stepping semi-implicit Runge-Kutta schemes were derived by treating nonstiff terms in the equations explicitly and simultaneously treating the stiff terms implicitly. These new algorithms has been tested to be more accurate than conventional implicit methods while maintaining the robustness of the calculations in [17].

In this paper, we present an efficient semi-implicit high-order finite difference algorithm and computation codes for the DNS of 3-D transient hypersonic stability and transition over blunt body. The govern-

1

ing equations are the 3-D compressible Navier-Stokes equations. The equations are discretized in space using the fifth-order upwind schemes which can be replaced by other high-order schemes if necessary. A high-order shock fitting numerical scheme developed in [18] is also used to treat the presence of shock waves. The spatial discretization terms of the governing equations are separated into stiff terms, involving derivatives along the wall-normal direction only, and nonstiff terms for the rest of the equations. The split equations are advanced in time using the semi-implicit temporal schemes, which lead to efficient computations of block seven-diagonal systems of implicit equations. The semi-implicit method is used to remove the stiffness caused by the small grid sizes along the wall-normal direction in the boundary layers. The restriction on the time step is only limited by the streamwise grid sizes and accuracy conditions.

Governing Equations

Although real gas effects become important as gas temperature increases for hypersonic flow behind a strong bow shock, perfect gas assumption is used in this paper. The method can be extended to nonequilibrium real-gas flow if necessary. The governing equations are the unsteady three-dimensional Navier-Stokes equations

$$\frac{\partial U}{\partial t} + \frac{\partial F_j}{\partial x_j} + \frac{\partial F_{vj}}{\partial x_j} = 0 \tag{1}$$

where

$$U = \{\rho, \rho u_1, \rho u_2, \rho u_3, e\} \tag{2}$$

$$F_j = \left\{ \begin{array}{c} \rho u_j \\ \rho u_1 u_j + p\delta_{1j} \\ \rho u_2 u_j + p\delta_{2j} \\ \rho u_3 u_j + p\delta_{3j} \\ (e + p) u_j \end{array} \right\} \tag{3}$$

$$F_{vj} = \left\{ \begin{array}{c} 0 \\ \tau_{1j} \\ \tau_{2j} \\ \tau_{3j} \\ \tau_{jk} u_k - q_j \end{array} \right\} \tag{4}$$

$$p = \rho R T \tag{5}$$

$$e = \rho(c_v T + \frac{\rho}{2} u_k u_k) \tag{6}$$

$$\tau_{ij} = -\mu \left(\frac{\partial u_i}{\partial x_j} + \frac{\partial u_j}{\partial x_i} \right) + 2\mu/3 \frac{\partial u_k}{\partial x_k} \delta_{ij} \tag{7}$$

$$q_j = -\kappa \frac{\partial T}{\partial x_j} \tag{8}$$

The general curvilinear three-dimensional coordinates (ξ, η, ζ, τ) are used along the body fitted grid lines (Fig. 1). Shock fitting methods are used to treat the bow shock as a computational boundary. The trans-

formation relations for the current grid systems are

$$\left\{ \begin{array}{l} \xi = \xi(x, y, z) \\ \eta = \eta(x, y, z, t) \\ \zeta = \zeta(x, y, z) \\ \tau = t \end{array} \right. \Longleftrightarrow \left\{ \begin{array}{l} x = x(\xi, \eta, \zeta, \tau) \\ y = y(\xi, \eta, \zeta, \tau) \\ y = y(\xi, \eta, \zeta, \tau) \\ t = \tau \end{array} \right. \tag{9}$$

where $\xi_t = 0$ and $\zeta_t = 0$ because the ξ and ζ grid lines are fixed when the shock boundary moves.

In the numerical simulations, the governing equations (1) are transformed into the computational domain (ξ, η, ζ, τ) as follows

$$\frac{1}{J} \frac{\partial U}{\partial \tau} + \frac{\partial E'}{\partial \xi} + \frac{\partial F'}{\partial \eta} + \frac{\partial G'}{\partial \zeta}$$
$$+ \frac{\partial E'_v}{\partial \xi} + \frac{\partial F'_v}{\partial \eta} + \frac{\partial G'_v}{\partial \zeta} + U \frac{\partial(\frac{1}{J})}{\partial \tau} = 0 \tag{10}$$

where

$$E' = \frac{F_1 \xi_x + F_2 \xi_y + F_3 \xi_z}{J} \tag{11}$$

$$F' = \frac{F_1 \eta_x + F_2 \eta_y + F_3 \eta_z + U \eta_t}{J} \tag{12}$$

$$G' = \frac{F_1 \zeta_x + F_2 \zeta_y + F_3 \zeta_z}{J} \tag{13}$$

$$E'_v = \frac{F_{v1} \xi_x + F_{v2} \xi_y + F_{v3} \xi_z}{J} \tag{14}$$

$$F'_v = \frac{F_{v1} \eta_x + F_{v2} \eta_y + F_{v3} \eta_z}{J} \tag{15}$$

$$G'_v = \frac{F_{v1} \zeta_x + F_{v2} \zeta_y + F_{v3} \zeta_z}{J} \tag{16}$$

where J is the Jacobian of the coordinate transformation, and ξ_x, ξ_y, ξ_z, η_x, η_y, η_z, η_t, ζ_x, ζ_y, and ζ_z are the grid transformation matrices. In the equations, the transformed inviscid fluxes E', F', and G' are standard flux terms with known eigenvalues and eigenvectors. The transport flux terms E'_v, F'_v, and G'_v contain both first-order and second-order spatial derivatives of velocity and temperature. These derivatives in the Cartesian coordinates (x, y, z) are transformed into the computational coordinates (ξ, η, ζ) using a chain rule for spatial discretization.

Numerical Method

In the current semi-implicit methods, the spatial discretization of the Navier-Storkes equations is additively split into the stiff terms involving spatial derivatives normal to the wall and the rest of the flux terms, which lead to a system of ordinary differential equations in the form of

$$\frac{d\mathbf{u}}{dt} = \mathbf{f}(t, \mathbf{u}) + \mathbf{g}(t, \mathbf{u}) \tag{17}$$

where $\mathbf{u}$ is the vector of discretized variables $\{U_{ij}\}_{i=1,\ldots,IL; j=1,\ldots,JL}$ in the flow field, $\mathbf{f}(t, \mathbf{u})$ represents the nonstiff term, and $\mathbf{g}(t, \mathbf{u})$ represents the stiff

American Institute of Aeronautics and Astronautics

term. The split ordinary differential equation (17) is then integrated in time using semi-implicit Runge-Kutta schemes derived by Zhong et al. [15] [19] or second-order AB-CN semi-implicit method, where $\mathbf{f}$ is treated explicitly and $\mathbf{g}$ is treated implicitly. The resulting semi-implicit methods for time-accurate computations of the Navier-Stokes quations are high-order accurate in both space and time, and they are much more efficient than the spatially full implicit schemes. The details of the method are presented in the following sections.

Spatial Discretization and Splitting

Though the high-order semi-implicit method is developed for DNS of 3-D boundary layers, only 2-D formulas are presented here. The extension to 3-D case is straightforward.

Equation (10) is additively split into relatively nonstiff part $\mathbf{f}(\mathbf{U}_{ij})$ and stiff part $\mathbf{g}(\mathbf{U}_{ij})$ as follows

$$\frac{1}{J}\frac{\partial \mathbf{U}_{ij}}{\partial t} = \mathbf{f}(\mathbf{U}_{ij}) + \mathbf{g}(\mathbf{U}_{ij}) \tag{18}$$

where J is Jacobian of the coordinate transformation and

$$\mathbf{f}(\mathbf{U}_{ij}) = -\frac{\partial E'}{\partial \xi} + \frac{\partial E'_v}{\partial \xi} + \frac{\partial F'_{v1}}{\partial \eta} \tag{19}$$

$$\mathbf{g}(\mathbf{U}_{ij}) = -\frac{\partial F'}{\partial \eta} + \frac{\partial F'_{v2}}{\partial \eta} \tag{20}$$

where F'_{v2} is the part of the viscous flux terms only involving normal derivatives, and F'_{v1} is the part of the viscous flux terms except F'_{v2}, i.e.,

$$\frac{\partial F'_v}{\partial \eta} = \frac{\partial F'_{v1}}{\partial \eta} + \frac{\partial F'_{v2}}{\partial \eta} \tag{21}$$

Generally, in Eq. (18), $\mathbf{g}(\mathbf{U}_{ij})$ is much stiffer than $\mathbf{f}(\mathbf{U}_{ij})$ because very small grid space is used in the wall-normal direction compared to that used in streamwise direction.

From Eq. (13)

$$\frac{\partial F'_v}{\partial \eta} = \frac{\partial}{\partial \eta}\left\{\frac{E_v \eta_x + F_v \eta_y}{J}\right\}$$

$$= \frac{\partial}{\partial \eta}\left\{\begin{array}{c} 0 \\ (\eta_x \tau_{11} + \eta_y \tau_{12})/J \\ (\eta_x \tau_{21} + \eta_y \tau_{22})/J \\ (\eta_x(\tau_{1k}u_k - q_1) + \eta_y(\tau_{2k}u_k - q_2))/J \end{array}\right\}$$

where $k = 1, 2$ and

$$\frac{\partial \tau_{11}}{\partial \eta} = \frac{\partial}{\partial \eta}\left\{\mu\left[\frac{4}{3}\left(\xi_x \frac{\partial u}{\partial \xi} + \eta_x \frac{\partial u}{\partial \eta}\right) - \frac{2}{3}\left(\xi_y \frac{\partial v}{\partial \xi} + \eta_y \frac{\partial v}{\partial \eta}\right)\right]\right\}$$

$$\frac{\partial \tau_{12}}{\partial \eta} = \frac{\partial}{\partial \eta}\left\{\mu\left[\xi_y \frac{\partial u}{\partial \xi} + \eta_y \frac{\partial u}{\partial \eta} + \xi_x \frac{\partial v}{\partial \xi} + \eta_x \frac{\partial v}{\partial \eta}\right]\right\}$$

$$\frac{\partial \tau_{22}}{\partial \eta} = \frac{\partial}{\partial \eta}\left\{\mu\left[\frac{4}{3}\left(\xi_y \frac{\partial v}{\partial \xi} + \eta_y \frac{\partial v}{\partial \eta}\right) - \frac{2}{3}\left(\xi_x \frac{\partial u}{\partial \xi} + \eta_x \frac{\partial u}{\partial \eta}\right)\right]\right\}$$

$$\frac{\partial q_1}{\partial \eta} = -\frac{\partial}{\partial \eta}\left\{k\left[\xi_x \frac{\partial T}{\partial \xi} + \eta_x \frac{\partial T}{\partial \eta}\right]\right\}$$

$$\frac{\partial q_2}{\partial \eta} = -\frac{\partial}{\partial \eta}\left\{k\left[\xi_y \frac{\partial T}{\partial \xi} + \eta_y \frac{\partial T}{\partial \eta}\right]\right\}$$

So,

$$\frac{\partial F'_{v2}}{\partial \eta} = \frac{\partial}{\partial \eta}\left(\frac{1}{J}\left\{\begin{array}{c} 0 \\ \tau_{\eta 2} \\ \tau_{\eta 3} \\ \tau_{\eta 4} \end{array}\right\}\right) \tag{22}$$

where

$$\tau_{\eta 2} = \mu\left(\frac{4}{3}\eta_x\eta_x + \eta_y\eta_y\right)\frac{\partial u}{\partial \eta}$$
$$+ \mu\left(-\frac{2}{3}\eta_y\eta_x + \eta_x\eta_y\right)\frac{\partial v}{\partial \eta}$$

$$\tau_{\eta 3} = \mu\left(\eta_y\eta_x - \frac{2}{3}\eta_x\eta_y\right)\frac{\partial u}{\partial \eta}$$
$$+ \mu\left(\eta_x\eta_x + \frac{4}{3}\eta_y\eta_y\right)\frac{\partial v}{\partial \eta}$$

$$\tau_{\eta 4} = u\tau_{\eta 2} + v\tau_{\eta 3} + k\left(\eta_x\eta_x + \eta_y\eta_y\right)\frac{\partial T}{\partial \eta}$$

For the inviscid flux vectors in the Eqs. (19) and (20), the flux Jacobians contain both positive and negative eigenvalues in general. A simple local Lax-Friedrichs scheme is used to split the inviscid flux vectors into positive and negative wave fields. For example, the flux term F' in Eq. (20) can be split into two terms of pure positive and negative eigenvalues as follows

$$F' = F'_+ + F'_- \tag{23}$$

where

$$F'_+ = \frac{1}{2}(F' + \lambda U) \tag{24}$$

$$F'_- = \frac{1}{2}(F' - \lambda U) \tag{25}$$

where λ is chosen to be larger than the local maximum eigenvalues of F'

$$\lambda = \frac{|\nabla \eta|}{J}\left(\sqrt{(\epsilon c)^2 + u'^2} + c\right) \tag{26}$$

where

$$u' = \frac{\eta_x u + \eta_y v + \eta_z w + \eta_t}{|\nabla \eta|} \tag{27}$$

The parameter ϵ is a small positive constant added for the smoothness of the splitting. The fluxes F'_+ and F'_-

3

contain only positive and negative eigenvalues respectively. Therefore, in the spatial discretization of Eq. (21), the flux derivatives are split into two terms

$$\frac{\partial F'}{\partial \eta} = \frac{\partial F'_+}{\partial \eta} + \frac{\partial F'_-}{\partial \eta} \qquad (28)$$

where the first term on the right hand side is discretized by an upwind high-order finite-difference method and the second term is discretized by a downwind high-order finite-difference method. Meanwhile, high order central difference schemes are used for the viscous flux terms.

The fifth-order upwind explicit schemes is

$$u'_i = \frac{1}{h\,b_i} \sum_{k=-3}^{3} a_{i+k}\, u_{i+k}$$
$$- \frac{\alpha}{6!\,b_i} h^5 \left(\frac{\partial u^6}{\partial^6 x}\right)_i + \cdots \qquad (29)$$

where

$$\begin{aligned}
a_{i\pm3} &= \pm 1 + \tfrac{1}{12}\alpha \\
a_{i\pm2} &= \mp 9 - \tfrac{1}{2}\alpha \\
a_{i\pm1} &= \pm 45 + \tfrac{5}{4}\alpha \\
a_i &= 0 - \tfrac{5}{3}\alpha \qquad\qquad b_i = 60
\end{aligned}$$

This scheme is fifth-order upwind scheme when $\alpha < 0$, and it is sixth-order central scheme when $\alpha = 0$. Corresponding sixth-order central explicit inner scheme for the second order derivatives is

$$u''_i = \frac{1}{90h^2}\left(u_{i-3} - \frac{17}{2}u_{i-2} + 135u_{i-1} - 245u_i\right.$$
$$\left. + 135u_{i+1} - \frac{17}{2}u_{i+2} + u_{i+3}\right) \qquad (30)$$

Semi-Implicit Schemes

Equation (17) can be integrated in time using high-order semi-implicit temporal schemes, where $\mathbf{f}$ is treated explicitly and $\mathbf{g}$ is treated implicitly. Three kinds of high-order semi-implicit Runge-Kutta schemes for high-order temporal integration of the governing equations for reacting flow simulations has been derived in [20, 21]. For example, 3rd order Rosenbrock Additive Semi-Implicit Runge-Kutta (ASIRK-3C) Method is:

$$\left\{\begin{aligned}
&[I - ha_1\mathbf{J}(\mathbf{u}^n)]\,\mathbf{k}_1 = h\{\mathbf{f}(\mathbf{u}^n) + \mathbf{g}(\mathbf{u}^n)\} \\
&[I - ha_2\mathbf{J}(\mathbf{u}^n + c_{21}\mathbf{k}_1)]\,\mathbf{k}_2 = \\
&\qquad\qquad h\{\mathbf{f}(\mathbf{u}^n + b_{21}\mathbf{k}_1) + \\
&\qquad\qquad \mathbf{g}(\mathbf{u}^n + c_{21}\mathbf{k}_1)\} \\
&[I - ha_3\mathbf{J}(\mathbf{u}^n + c_{31}\mathbf{k}_1 + c_{32}\mathbf{k}_2)]\,\mathbf{k}_3 = \\
&\qquad\qquad h\{\mathbf{f}(\mathbf{u}^n + b_{31}\mathbf{k}_1 + b_{32}\mathbf{k}_2) + \\
&\qquad\qquad \mathbf{g}(\mathbf{u}^n + c_{31}\mathbf{k}_1 + c_{32}\mathbf{k}_2)\} \\
&\mathbf{u}^{n+1} = \mathbf{u}^n + \omega_1\mathbf{k}_1 + \omega_2\mathbf{k}_2 + \omega_3\mathbf{k}_3
\end{aligned}\right. \qquad (31)$$

where

$$\omega_1 = \tfrac{1}{8} \qquad \omega_2 = \tfrac{1}{8} \qquad \omega_3 = \tfrac{3}{4}$$

$$\begin{aligned}
b_{21} &= \tfrac{8}{7} & b_{31} &= \tfrac{71}{252} & b_{32} &= \tfrac{7}{36} \\
a_1 &= .797097 & a_2 &= .591381 & a_3 &= .134705 \\
c_{21} &= 1.05893 & c_{31} &= \tfrac{1}{2} & c_{32} &= -.375939
\end{aligned}$$

where a_1, a_2, a_3, c_{21}, and c_{32} are irrational numbers with six significant digits. The parameters of the semi-implicit Runge-Kutta methods are chosen based on both stability and accuracy requirements with the simultaneous coupling between the explicit and implicit terms. Corresponding high-order low-storage semi-implicit Runge-Kutta method versions and coefficients (LSSIRK-2C, LSSIRK-3C) can be found in [19].

Second-order AB-CN method, which uses a combined Crank-Nicolson method and Adams-Bashford method, can be written as

$$\begin{aligned}
\mathbf{u}^{n+1} = \;&\mathbf{u}^n + \frac{h}{2}\left[3\mathbf{f}(\mathbf{u}^n) - \mathbf{f}(\mathbf{u}^{n-1})\right] \\
&+ \frac{h}{2}\left[\mathbf{g}(\mathbf{u}^n) + \mathbf{g}(\mathbf{u}^{n+1})\right]
\end{aligned} \qquad (32)$$

Jacobians for Semi-implicit Schemes

In order to apply the semi-implicit schemes to the Eq.(18), Jacobian matrices $\mathbf{J}(\mathbf{u}) = \partial\mathbf{g}/\partial\mathbf{u}$ are needed in the Eqs. (31) and (32). In order to maintain high-order temporal accuracy, the derivative of the viscosity coefficient with respect to temperature needs to be included in the Jacobian. The components of the Jacobian $\mathbf{J}(\mathbf{u})$ are derived as follows

$$\delta\mathbf{g}(U_{ij}) = \delta\left(-\frac{DF'_+}{D\eta} - \frac{DF'_-}{D\eta} + \frac{DF'_{v2}}{D\eta}\right)_{ij} \qquad (33)$$

where $D/D\eta$ is the fifth-order finite difference approximation of the derivatives only in wall-normal direction, and F'_+, F'_- are inviscid fluxes from Eq. (28).

a. Inviscid Flux Jacobian

The Jacobian for inviscid flux is

$$\delta F'_\pm(U)^n = \frac{\partial F'_\pm}{\partial U}\delta U^n \qquad (34)$$

where

$$\frac{\partial F'_\pm}{\partial U} = \frac{\partial\left(\frac{1}{2}(F' \pm \lambda U)\right)}{\partial U} \qquad (35)$$

b. Viscous Flux Jacobian

The Jacobian for viscous flux in the implicit part is

$$\begin{aligned}
\delta F'_{v2} =\;& \mathbf{A_v}\frac{\partial^2}{\partial\eta^2}(\delta V) + \mathbf{B_v}\frac{\partial}{\partial\eta}(\delta V) + \mathbf{C_v}\delta V \\
=\;& \mathbf{A_v}\frac{\partial^2}{\partial\eta^2}\left(\frac{\partial V}{\partial U}\delta U\right) + \mathbf{B_v}\frac{\partial}{\partial\eta}\left(\frac{\partial V}{\partial U}\delta U\right) \\
&+ \mathbf{C_v}\frac{\partial V}{\partial U}\delta U
\end{aligned} \qquad (36)$$

4

where

$$V = \begin{bmatrix} \rho \\ u \\ v \\ T \end{bmatrix} \quad \frac{\partial V}{\partial U} = \begin{bmatrix} 1 & 0 & 0 & 0 \\ \frac{u}{\rho} & \frac{1}{\rho} & 0 & 0 \\ \frac{v}{\rho} & 0 & \frac{1}{\rho} & 0 \\ \frac{\alpha - e_i}{\rho C_v} & -\frac{u}{\rho C_v} & -\frac{v}{\rho C_v} & \frac{1}{\rho C_v} \end{bmatrix}$$ (37)

$$\mathbf{A_v} = \frac{1}{J} \begin{bmatrix} 0 & 0 & 0 & 0 \\ 0 & \mu a_{22} & \mu a_{23} & 0 \\ 0 & \mu a_{23} & \mu a_{33} & 0 \\ 0 & a_{42} & a_{43} & k a_{44} \end{bmatrix}$$ (38)

$$\mathbf{B_v} = \frac{1}{J} \begin{bmatrix} 0 & 0 & 0 & 0 \\ 0 & \frac{\partial \mu}{\partial \eta} a_{22} & \frac{\partial \mu}{\partial \eta} a_{23} & b_{24} \\ 0 & \frac{\partial \mu}{\partial \eta} a_{23} & \frac{\partial \mu}{\partial \eta} a_{33} & b_{34} \\ 0 & b_{42} & b_{43} & b_{44} \end{bmatrix}$$ (39)

$$\mathbf{C_v} = \frac{1}{J} \begin{bmatrix} 0 & 0 & 0 & 0 \\ 0 & 0 & 0 & c_{24} \\ 0 & 0 & 0 & c_{34} \\ 0 & c_{42} & c_{43} & c_{44} \end{bmatrix}$$ (40)

where

$$\alpha = \frac{1}{2}\left(u^2 + v^2\right)$$
$$e_i = C_v T$$

Coefficients in the matrices of $\mathbf{A_v}$, $\mathbf{B_v}$ and $\mathbf{C_v}$ can be found in appendix.

c. Implicit Jacobian Matrix

The Jacobian matrix for the implicit parts can be obtained from Eqs. (35) and (36) after applying the same fifth-order upwind scheme and central scheme described in Eqs. (29) and (30).

$$\delta \mathbf{g}(U_{ij}) = A_{ij} \delta U_{ij-3} + B_{ij} \delta U_{ij-2} + C_{ij} \delta U_{ij-1}$$
$$+ D_{ij} \delta U_{ij} + E_{ij} \delta U_{ij+1} + F_{ij} \delta U_{ij+2}$$
$$+ G_{ij} \delta U_{ij+3}$$ (41)

where

$$A_{ij} = a_1{}^1 \left(\frac{\partial F'_+}{\partial U}\right)_{ij-3} + a_1{}^2 \left(\frac{\partial F'_-}{\partial U}\right)_{ij-3}$$
$$- b_1{}^3 A_v \left(\frac{\partial V}{\partial U}\right)_{ij-3} - a_1{}^3 B_v \left(\frac{\partial V}{\partial U}\right)_{ij-3}$$

$$B_{ij} = a_2{}^1 \left(\frac{\partial F'_+}{\partial U}\right)_{ij-2} + a_2{}^2 \left(\frac{\partial F'_-}{\partial U}\right)_{ij-2}$$
$$- b_2{}^3 A_v \left(\frac{\partial V}{\partial U}\right)_{ij-2} - a_2{}^3 B_v \left(\frac{\partial V}{\partial U}\right)_{ij-2}$$

$$C_{ij} = a_3{}^1 \left(\frac{\partial F'_+}{\partial U}\right)_{ij-1} + a_3{}^2 \left(\frac{\partial F'_-}{\partial U}\right)_{ij-1}$$
$$- b_3{}^3 A_v \left(\frac{\partial V}{\partial U}\right)_{ij-1} - a_3{}^3 B_v \left(\frac{\partial V}{\partial U}\right)_{ij-1}$$

$$D_{ij} = a_4{}^1 \left(\frac{\partial F'_+}{\partial U}\right)_{ij} + a_4{}^2 \left(\frac{\partial F'_-}{\partial U}\right)_{ij}$$

$$- b_4{}^3 A_v \left(\frac{\partial V}{\partial U}\right)_{ij} - a_4{}^3 B_v \left(\frac{\partial V}{\partial U}\right)_{ij}$$
$$- C_v \left(\frac{\partial V}{\partial U}\right)_{ij}$$

$$E_{ij} = a_5{}^1 \left(\frac{\partial F'_+}{\partial U}\right)_{ij+1} + a_5{}^2 \left(\frac{\partial F'_-}{\partial U}\right)_{ij+1}$$
$$- b_5{}^3 A_v \left(\frac{\partial V}{\partial U}\right)_{ij+1} - a_5{}^3 B_v \left(\frac{\partial V}{\partial U}\right)_{ij+1}$$

$$F_{ij} = a_6{}^1 \left(\frac{\partial F'_+}{\partial U}\right)_{ij+2} + a_6{}^2 \left(\frac{\partial F'_-}{\partial U}\right)_{ij+2}$$
$$- b_6{}^3 A_v \left(\frac{\partial V}{\partial U}\right)_{ij+2} - a_6{}^3 B_v \left(\frac{\partial V}{\partial U}\right)_{ij+2}$$

$$G_{ij} = a_7{}^1 \left(\frac{\partial F'_+}{\partial U}\right)_{ij+3} + a_7{}^2 \left(\frac{\partial F'_-}{\partial U}\right)_{ij+3}$$
$$- b_7{}^3 A_v \left(\frac{\partial V}{\partial U}\right)_{ij+3} - a_7{}^3 B_v \left(\frac{\partial V}{\partial U}\right)_{ij+3}$$

where $a_l{}^1$, $a_l{}^2$, $b_l{}^3$, $a_l{}^3$ $(l = 1, \ldots, 7)$ are the coefficients of high-order schemes. The upperscript $1, 2, 3$ represent the upwind, downwind and central scheme respectively.

The final global Jacobian matrix for the implicit terms in the semi-implicit Runge-Kutta schemes is a block seven-diagonal matrix involving terms along the j grid direction only. The block seven-diagonal system of equations can be solved efficiently by a banded matrix solver.

Numerical Results

Numerical codes have been written by using high-order semi-implicit schemes with a high-order shock fitting algorithm. The spatial discretization is using fifth-order upwind scheme which can be replaced by other high-order schemes easily if necessary. The shock fitting procedure is turned off if there is no shock in the flow field.

1. Stiffness Analysis of a Linearized Model Equation

A two-dimensional linearized model convection-diffusion equation bounded by two parallel walls is

$$\frac{\partial u}{\partial t} + \frac{\partial u}{\partial x} + \frac{\partial u}{\partial y} = \frac{1}{R}\left(\frac{\partial^2 u}{\partial x^2} + \frac{\partial^2 u}{\partial x \partial y} + \frac{\partial^2 u}{\partial y^2}\right)$$ (42)

where R is the "Reynolds number". The boundary conditions are $u(x, 0) = u(x, 1) = 0$. When R is large, there is a thin viscous boundary layer on the wall with large gradients in y direction. This equation is used to do stiff analysis on the stiff terms and nonstiff terms of the model equation.

Similar to semi-implicit method of Navier-Stokes equations presented in previous section, the finite difference discretization of the spatial derivatives leads to a system of semi-discrete ordinary different equations,

i.e.

$$\frac{du_{ij}}{dt} = \mathbf{f}(u_{ij}) + \mathbf{g}(u_{ij}) \qquad (43)$$

where

$$\mathbf{f}(u_{ij}) = \left\{ -\frac{\partial u}{\partial x} + \frac{1}{R}\left(\frac{\partial^2 u}{\partial x^2} + \frac{\partial^2 u}{\partial x \partial y}\right)\right\}_{ij} \qquad (44)$$

$$\mathbf{g}(u_{ij}) = \left\{ -\frac{\partial u}{\partial y} + \frac{1}{R}\left(\frac{\partial^2 u}{\partial y^2}\right)\right\}_{ij} \qquad (45)$$

where explicit third-order upwind approximation is used for u_x, u_y and fourth-order central difference approximation is used for other terms. We can get

$$\frac{d\mathbf{U}}{dt} = [\mathbf{A}]\,\mathbf{U} + [\mathbf{B}]\,\mathbf{U} \qquad (46)$$

where $\mathbf{U}$ is a big matrix which includes all points in the computational domain, $[\mathbf{A}]$ is the big coefficient matrix of nonstiff term $\mathbf{f}(u_{ij})$, and $[\mathbf{B}]$ is the big coefficient matrix of stiff term $\mathbf{g}(u_{ij})$. By analysising the eigenvalue λ_f of $[\mathbf{A}]$ and the the eigenvalue λ_g of $[\mathbf{B}]$, we can get the information about the stiffness of $\mathbf{g}(u_{ij})$. The larger the ratio of $\frac{max|\lambda_g|}{max|\lambda_f|}$, the stiffer the $\mathbf{g}(u_{ij})$.

A periodic boundary condition is used in the x direction. A three-point extrapolation is used at the walls to calculate u located at one grid-point outside of the walls. Although stretched grids are often used in practice, simple uniform grids are used here. The conditions for the calculation are: $R = 10 \sim 40$, $R\Delta y = 0.25 \sim 1.0$, $\Delta x = 20$. The computation uses a set of 11×11 grids.

Figure 2 shows the changing of the ratio of $\frac{max|\lambda_g|}{max|\lambda_f|}$ along with Reynolds number changing. From the figure, the $\mathbf{g}(u_{ij})$ term is much stiffer than the $\mathbf{f}(u_{ij})$ term due to the big value of $\frac{max|\lambda_g|}{max|\lambda_f|}$, and the larger the R, the stiffer the $\mathbf{g}(u_{ij})$. When R is fixed, the smaller the Δy, the stiffer the the $\mathbf{g}(u_{ij})$. Semi-implicit methods can be applied when the stiff term is much stiffer than the nonstiff term.

2. Supersonic Couette Flow Stability (2-D)

Compressible Couette flow is a wall-bounded parallel shear flow which is a simple example of hypersonic shear flows. Because the mean flow is a parallel flow, the linear stability analysis based on the full Navier-Stokes equations does not involve the parallel approximation of a developing boundary layer. The LST results for compressible Couette flow are taken from [22]. Both steady and unsteady two-dimensional computations are tested.

Steady Flow Solutions

We first used the high-order semi-implicit Navier-Stokes codes to compute the steady solutions of the supersonic Couette flow. The results are compared with

Table 1: Numerical errors for computations of supersonic Couette flow using 5th-order semi-implicit scheme. ($e_1 = ||e||_1$ and $e_2 = ||e||_2$)

Grids	$e_1 \times 10^{-6}$	ratio	$e_2 \times 10^{-6}$	ratio
51	6.9913	–	1.4114	–
101	0.2315	30.2	0.034	41.5

"exact" solutions obtained by a shooting method with several order of magnitudes smaller errors. Several test cases with different Mach number, Reynolds number and wall temperature have been tested. The results shown in this paper are those for the following flow conditions: $M_\infty = 2$, the upper wall is an isothermal wall with $T_\infty = 220.66667K$ while the lower wall is an adiabatic wall. The gas is assumed perfect gas with $\gamma = 1.4$ and $Pr = 0.72$. The viscosity coefficient is calculated by the Sutherland's law

$$\mu = T^{3/2}\left(\frac{1+C}{T+C}\right) \qquad (47)$$

where C is taken to be 0.5.

Figure 3 shows the steady velocity and temperature profile obtained by using a semi-implicit fifth-order upwind scheme with 101 uniform grid points. The numerical results agree well with the exact solutions.

The numerical simulations are conducted using several sets of uniform grids in order to evaluate the accuracy of the algorithm. The quantitative numerical errors of the simulations using two kinds of uniform grids are listed in Table 1. The table shows that the numerical errors for this fifth-order semi-implicit scheme in spatial discretization are of the order of 10^{-6} using 51 grid points and 2.315×10^{-7} using 101 grid points.

The theoretical ratio of the errors between the coarse grids and the fine grids are 32 for a fifth-order scheme. The results in the table show that the numerical algorithms are able to maintain such high orders of accuracy.

Unsteady Flow Solutions

We conduct numerical simulations for the temporal stability of the compressible Couette flow by simulating the development of given initial disturbances in the 2-D flow field (shown in Fig. 4). The initial conditions are the steady flow solutions plus disturbances given by a set of eigenfunctions obtained by linear stability analysis. For small initial disturbances, the growth or decay of the disturbances is given by the eigenvalue of the eigen-mode. The unsteady flow field is solved by computing the unsteady Navier-Stokes equations using different kinds of semi-implicit temporal discretizations. The same stretched grids are used in y direction as those used in the LST calculation. The computational domain in the simulation is one period in length in the x

6

direction and periodic boundary conditions are used.

a. Stable Mode Disturbance Waves

The flow conditions of the first case are: $M_\infty = 2$ and $Re_\infty = 1000$. For this case, the initial disturbance wave has a dimensionless wave number of $\alpha = 3$, and the eigenvalue obtained from the temporal linear stability analysis is

$$\begin{aligned} \omega &= \omega_r + \omega_i i \\ &= 5.52034015848 - 0.132786378788i \end{aligned} \quad (48)$$

where a negative ω_i means that the disturbances will decay in time with a dimensionless frequency of ω_r.

We have applied full explicit 5th-order numerical method and three kinds of semi-implicit temporal discretizations, ASIRK-1C, LSSIRK-2C and LSSIRK-3C to this problem. Figure 5 shows the accuracy comparison among these numerical methods after running codes to the end of about two wave periods. Because full explicit method uses very small Δt in every time step, it can arrive high accuracy although we use 1st-order temporal discretization. Semi-implicit methods use larger Δt every time step. They lose some accuracy if 1st-order temporal discretization is still used. This need high-order treatment in temporal discretization. As shown in the figure, there are small differences of relative errors between the LSSIRK-2C and LSSIRK-3C methods whose relative errors are close to those of full explicit method. At this time, the numerical errors mainly come from the spatial discretization.

We run these codes to the end of two wave periods and record the real CPU time consuming of these numerical methods. Table 2 shows the comparison among these methods. The computational efficiency is improved by using semi-implicit methods compared with full explicit method. LSSIRK-2C and LSSIRK-3C method increase the CPU time consuming since they need more time to solve the big banded matrices, however, as shown above, they improve the accuracy of the numerical results.

Figure 6 and Figure 7 show the comparison of the DNS results using LSSIRK-2C method and the LST prediction for the time history of velocity perturbations, pressure and temperature perturbations respectively at a fixed point in the 2-D supersonic Couette flow field. The computation uses 52×101 stretching grids. The disturbance wave decayed along with time growing. Figure 8 show the distribution of instantaneous flow perturbations in the y direction at the end of about six wave periods. These figures show that the instantaneous perturbations of all flow variables for the 2-D numerical simulations by using semi-implicit method agree well with the LST results.

For sufficiently low amplitude waves, integration of the perturbation kinetic energy of the solutions ought to exhibit the exponential behavior:

$$E(t) = E_0 \epsilon^{2\omega_i t} \quad (49)$$

where E_0 is the perturbation energy at $t = 0$. Figure 9 display the time dependence of the logarithm of the computed perturbation energy divided by the initial perturbation energy in one wave period. Again the results agree well between the DNS results and the LST results.

b. Unstable Mode Disturbance Waves

The unstable mode in high Mach number and high Reynolds number supersonic Couette flow field can be obtained by using LST analysis [22] chosing the flow conditions of $M_\infty = 5$, $Re_\infty = 1.5 \times 10^5$, dimensionless wave number $\alpha = 3.2$, and the eigenvalue $\omega = \omega_r + \omega_i i = 0.27739555 + 0.00100708i$. In here, a positive ω_i means that the disturbances will increase in time with a dimensionless frequency of ω_r. Figure 10 shows a set of eigenfunctions of this eigenvalue obtained by linear stability analysis and Fig. 11 shows the contours of wave patterns of $Re(p')$.

The computation uses 52×151 stretching grids. Figure 12 and Figure 13 show the comparison between the DNS results using LSSIRK-2C method and the LST prediction for the time history of velocity perturbations, pressure and temperature perturbations at a fixed point in the flow field respectively. The disturbance waves are amplified along with time growing. For this higher Mach number and higher Reynolds number supersonic Couette flow stability problem, the DNS results agree well with the LST results.

3. Supersonic Boundary Layer Stability (2-D)

The fifth-order semi-implicit codes for 2-D unsteady Navier-Stokes equations are also applied to simulate the temporal stability of supersonic flat plate boundary layer. From the experience of simulating supersonic Couette stability, LSSIRK-2C semi-implicit method is used for current case. The initial conditions are the steady flow solutions plus disturbances given by a set of eigenfunctions obtained by linear stability analysis.

The computation uses 42×141 stretching grids. Figure 14 and Figure 15 display the mean flow of numerical results compared with the "exact" solutions obtained by a shooting method with several order of magnitudes smaller errors. The numerical results agree well with the exact solutions.

To obtain the unstable second mode disturbance, the flow conditions are chosen as followings: $M_\infty = 4.5$, Reynolds number $R = 1000$ (based on the boundary-layer length scale), initial disturbance wave number $\alpha = 0.22$ according to [23], and the eigenvalue obtained from the temporal linear stability analysis is

$$\begin{aligned} \omega &= \omega_r + \omega_i i \\ &= 25.77363556598 + 0.2497128329918i \end{aligned} \quad (50)$$

Figure 16 shows a set of eigenfunctions of this eigenvalue obtained by linear stability analysis and Fig. 17

7

shows the contours of wave patterns of $Re(p')$.

Figure 18 shows the comparison of the DNS results and the LST prediction for the time history of velocity perturbations at a fixed point in the 2-D supersonic flat plate boundary layer field. Again, the disturbance wave was amplified in time. Figure 19 shows the distribution of instantaneous flow perturbations in the y direction at the end of about three periods in time. The results agree well between the DNS results and the LST results.

Table 3 shows the comparision of records of real CPU time consuming between the semi-implicit method and the full explicit method after running the codes to the end of two time wave periods. The computational efficiency can be improved by using semi-implicit method compared with the full explicit method.

4. Receptivity of A Hypersonic Boundary Layer

The last test case considered for validating is the numerical simulation of the receptivity of a two-dimensional boundary layer to weak freestream acoustic disturbance waves for hypersonic flow past a parabolic leading edge at zero angle of attack. In this spatial test case, we use the same the flow conditions and same boundary conditions as those in [24]. The purpose of the test case is to evaluate the numerical efficiency and accuracy of such simulations of the steady and unsteady cases using the new high-order semi-implicit method with a set of 160×120 grids.

The specific flow conditions are

$$
\begin{array}{ll}
M_\infty = 15 & \epsilon = 5 \times 10^{-4} \\
T_\infty^* = 192.989\,K & p_\infty^* = 10.3\,Pa \\
T_w^* = 1000\,K & \gamma = 1.4 \\
R^* = 286.94\,Nm/kgK & Pr = 0.72 \\
b^* = 40\,m^{-1} & d^* = 0.1\,m \\
T_r^* = 288\,K & T_s^* = 110.33\,K \\
\mu^* = 0.17894 \times 10^{-4} kg/ms
\end{array}
$$

Nose Radius of Curvature $= r^* = 0.0125\,m$
$Re_\infty = \rho_\infty^* U_\infty^* d^* / \mu_\infty^* = 6026.55$

The body surface is a parabola given by

$$x^* = b^* y^{*2} - d^* \tag{51}$$

where b^* a given constant and d^* is taken as the reference length. The body surface is assumed to be a non-slip wall with an isothermal wall temperature T_w^*.

In the simulation, the freestream disturbances are superimposed on the steady mean flow to investigate the development of T-S waves in the boundary layer with the effects of the bow shock interaction. The freestream disturbances are assumed to be weak monochromatic planar acoustic waves with wave front normal to the center line of the body. The perturbations of flow variable introduced by the freestream acoustic wave before reaching the bow shock can be written in the following

form

$$
\left\{ \begin{array}{c} u' \\ v' \\ p' \\ \rho' \end{array} \right\}_\infty = \left\{ \begin{array}{c} |u'| \\ |v'| \\ |p'| \\ |\rho'| \end{array} \right\}_\infty e^{ik[x-(1+M_\infty^{-1})t]} \tag{52}
$$

where $|u'|$, $|u'|$, $|p'|$, and $|\rho'|$ are perturbation amplitudes satisfying the following relations

$$
\begin{array}{ll}
|u'|_\infty = \epsilon, & |v'|_\infty = 0 \\
|p'|_\infty = \gamma M_\infty \epsilon, & |\rho'|_\infty = M_\infty \epsilon
\end{array}
$$

where ϵ is a small number representing the freestream wave magnitude. The parameter k is the dimensionless freestream wave number which is related to the dimensionless circular frequency ω by

$$\omega = k\left(1 + M_\infty^{-1}\right) \tag{53}$$

The corresponding dimensionless frequency F is defined as

$$F = \frac{\omega^* \nu^*}{U_\infty^{*2}} = \omega / Re_\infty. \tag{54}$$

Steady Flow Solutions

The steady flow solutions of the Navier-Stokes equations for the viscous hypersonic flow over the parabola are obtained by using second order AB-CN semi-implicit temporal discretization along with fifth order spatial discretization and advance the solutions to a steady state without freestream perturbations. Figure 20 shows steady flow solutions for a set of 160×120 computational grids, pressure contours, and temperature contours.

The numerical accuracy of the semi-implicit method is evaluated by comparing the solutions with those of full explicit method. Figures 21 compare the pressure profile behind the bow shock shape and the pressure on the body surface between these two numerical methods. Figure 22 shows the comparison for Mach number along the stagnation line. All these steady solutions show that the results of semi-implicit method agree with the results of full explicit method well. Accurate steady solutions can be obtained by running high-order semi-implicit method.

Unsteady Flow Solutions

In this section, the generation of boundary-layer T-S and inviscid instability waves by freestream acoustic disturbances is considered for hypersonic flow over a parabolic leading edge with freestream disturbance wave numbers $k = 15$. The corresponding dimensionless frequency $F \times 10^{-6}$ is 2655. Efficiency and accuracy of the new semi-implicit method code are studied again for this unsteady receptivity problem.

Figure 23 shows the contours for the instantaneous perturbation u' of the velocity in x direction after the

American Institute of Aeronautics and Astronautics

flow field reaching a periodic state, the Fourier amplitude $| u' |$ and the phase angle $\varphi_{u'}$ (in degrees). The numerical solutions are obtained by using high-order semi-implicit method with a set of 160×120 grids. The unsteady computations are run for more than 29 periods in time to ensure that periodic solutions have been reached for the entire flow field. The instantaneous contours of u' show the development of instability waves in the boundary layer on the surface. The first region of $x < 0.2$ dominated by the first mode instability and the second region of $x > 0.2$ dominated by the second mode instability were numerically obtained by using semi-implicit method. These regions have been discussed in [24] by using high-order full explicit method. From the contours of the Fourier amplitudes and phase angles for u' in Fig. 23, the characteristics of the switching of instability modes from region 1 to region 2, the decay of first mode and the growth of the second mode with the sudden phase angle change near the body surface around $x = 0.2$ are also captured by using the new semi-implicit method.

Figures 24 and 25 compare the distribution of instantaneous entropy perturbations along the parabola surface and behind the bow shock surface respectively. The results agree well between the semi-implicit method and full explicit method. Meanwhile, the comparison of the distribution of the Fourier amplitudes and phase angles of the instantaneous entropy perturbations along the parabola surface are shown in Fig. 26 and Fig. 27 respectively. High-order semi-implicit method can arrive the same accuracy as the full explicit method if we apply high-order semi-implicit temporal discretization.

Table 4 shows the real CPU time consuming comparison between the full explicit method and the second order AB-CN semi-implicit method. The real CPU time is recorded by running the code for about 10 wave periods. The magnitude of the maximum time step used in numerical calculation is limited by the stability condition related to the grid size in the streamwise direction. The stiffness of fine grids in the direction across the boundary layers is overcome by the semi-implicit method. The computation results show the new schemes improved the computational efficiency nearly one order of magnitude compared with the full explicit methods.

Again, these results show that the current unsteady simulations with high-order semi-implicit method are highly accurate and highly efficient for hypersonic boundary layer DNS studies.

Summary

An efficient high-order semi-implicit Runge-Kutta method has been presented for computing the stability and transition of hypersonic boundary layers using the unsteady Navier-Stokes equations. The method uses semi-implicit treatment to overcome the stiffness of viscous wall-normal derivative terms, while the streamwise terms are computed by explicit methods for efficient unsteady flow calculations. The efficiency and accuracy of the method has been tested in several cases. The results show that by using the semi-implicit method, the computational efficiency can be improved nearly one order of magnitude while maintaining the same accuracy as full explicit method. The CFL numbers in the semi-implicit computations are only limited by streamwise grid space and the accuracy requirement for unsteady flow computations.

Acknowledgments

Appendix

In this section, coefficients of viscous flux Jacobian for semi-implicit schemes are presented.

$$a_{22} = \frac{4}{3}\eta_x\eta_x + \eta_y\eta_y$$

$$a_{23} = -\frac{2}{3}\eta_y\eta_x + \eta_x\eta_y$$

$$a_{33} = \eta_x\eta_x + \frac{4}{3}\eta_y\eta_y$$

$$a_{42} = \mu\left(a_{22}u + a_{23}v\right)$$

$$a_{43} = \mu\left(a_{23}u + a_{33}v\right)$$

$$a_{44} = \eta_x{}^2 + \eta_y{}^2$$

$$b_{24} = a_{22}\frac{\partial u}{\partial \eta}\frac{\partial \mu}{\partial T} + a_{23}\frac{\partial v}{\partial \eta}\frac{\partial \mu}{\partial T}$$

$$b_{34} = a_{23}\frac{\partial u}{\partial \eta}\frac{\partial \mu}{\partial T} + a_{33}\frac{\partial v}{\partial \eta}\frac{\partial \mu}{\partial T}$$

$$b_{42} = a_{22}\left(2\mu\frac{\partial u}{\partial \eta} + u\frac{\partial \mu}{\partial \eta}\right) + a_{23}\left(2\mu\frac{\partial v}{\partial \eta} + v\frac{\partial \mu}{\partial \eta}\right)$$

$$b_{43} = a_{23}\left(2\mu\frac{\partial u}{\partial \eta} + u\frac{\partial \mu}{\partial \eta}\right) + a_{33}\left(2\mu\frac{\partial v}{\partial \eta} + v\frac{\partial \mu}{\partial \eta}\right)$$

$$b_{44} = u\frac{\partial \mu}{\partial T}\left(a_{22}\frac{\partial u}{\partial \eta} + a_{23}\frac{\partial v}{\partial \eta}\right) + v\frac{\partial \mu}{\partial T}\left(a_{23}\frac{\partial u}{\partial \eta}\right.$$
$$\left. + a_{33}\frac{\partial v}{\partial \eta}\right) + 2a_{44}\frac{\partial k}{\partial \eta}$$

$$c_{24} = a_{22}\frac{\partial^2 u}{\partial \eta^2}\frac{\partial \mu}{\partial T} + a_{23}\frac{\partial^2 v}{\partial \eta^2}\frac{\partial \mu}{\partial T}$$

$$c_{34} = a_{23}\frac{\partial^2 u}{\partial \eta^2}\frac{\partial \mu}{\partial T} + a_{33}\frac{\partial^2 v}{\partial \eta^2}\frac{\partial \mu}{\partial T}$$

$$c_{42} = a_{22}\frac{\partial}{\partial \eta}\left(\mu\frac{\partial u}{\partial \eta}\right) + a_{23}\frac{\partial}{\partial \eta}\left(\mu\frac{\partial v}{\partial \eta}\right)$$

$$c_{43} = a_{23}\frac{\partial}{\partial \eta}\left(\mu\frac{\partial u}{\partial \eta}\right) + a_{33}\frac{\partial}{\partial \eta}\left(\mu\frac{\partial v}{\partial \eta}\right)$$

9

$$c_{44} = a_{22}\frac{\partial\mu}{\partial T}\frac{\partial}{\partial\eta}\left(u\frac{\partial u}{\partial\eta}\right) + a_{33}\frac{\partial\mu}{\partial T}\frac{\partial}{\partial\eta}\left(v\frac{\partial u}{\partial\eta}\right)$$
$$+a_{23}\frac{\partial\mu}{\partial T}\frac{\partial}{\partial\eta}\left(v\frac{\partial u}{\partial\eta} + u\frac{\partial v}{\partial\eta}\right) + a_{44}\frac{\partial^2 T}{\partial\eta^2}\frac{\partial k}{\partial T}$$

References

[1] National Research Council (U.S.). Committee on Hypersonic Technology for Military Application, "Hypersonic Technology for Military Application," *Technical Report*, Vol. National Academy Press, Washington, DC., 1989.

[2] Erlebacher, G. and Hussaini, M. Y., "Numerical experiments in supersonic boundary-layer stability," *Physics of Fluids: A*, Vol. 2, 1990, pp. 94–104.

[3] Ng, L. L. and Erlebacher, G., "Secondary Instability in Compressible Boundary Layers," *Physics of Fluids: A*, Vol. 4, 1992, pp. 710–717.

[4] Thumm, A., Wolz, W., and Fasel, H., "Numerical Simulation of Spatially Growing Three-Dimensional Disturbance Waves in Compressible Boundary Layers," *in Laminar-Turbulent Transition, IUTAM Symposium, Toulouse, France, 1989, D. Arnal, R. Michel, Editors*, Vol. Springer-Verlag Berlin, 1990.

[5] Fasel, H., Trumm, A., and Bestek, H., "Direct Numerical Simulation of Transition in Supersonic Boundary Layer: Oblique Breakdown," *Transitional and Turbulent Compressible Flows, ASME FED-Vol. 151*, 1993.

[6] Eibler, W. and Bestek, H., "Spatial Numerical Simulations of Linear and Weakly Nonlinear Instabilities in Supersonic Boundary Layers," *Theoretical and Computational Fluid Dynamics*, Vol. Vol. 8, pp. 219-235, 1996.

[7] Adams, N. A. and Kleiser, L., "Numerical Simulation of Transition in a Compressible Flat Plate Boundary Layer," *Transitional and Turbulent Compressible Flows, ASME FED-Vol. 151*, 1993.

[8] Adams, N. A., "Subharmonic Transition to Turbulence in a Flat-Plate Boundary Layer at Mach Number 4.5," *Journal of Fluid Mechanics*, Vol. Vol. 317, pp. 301–335, 1996.

[9] Guo, Y., Adams, N. A., Sandham, N. D., and Kleiser, L., "Numerical Simulation of Supersonic Boundary Layer Transition," *Application of Direct and Large Eddy Simulation to Transition and Turbulence*, Vol. AGARD-CP-551, 1994.

[10] Reed, H. L., "Direct Numerical Simulation of Transition: the Spatial Approach," *Progress in Transition Modeling*, AGARD-Report-793 1994.

[11] Pruett, C. D. and Chang, C. L., "A Comparison of PSE and DNS for High-Speed Boundary-Layer Flows," *Transitional and Turbulent Compressible Flows*, Vol. L. D. Kral and T. A. Zang, editors, pp. 57-67, FED-Vol. 151, ASME, 1993.

[12] Pruett, C. D., Zang, T. A., Chang, C.-L., and Carpenter, M. H., "Spatial Direct Numerical Simulation of High-Speed Boundary-Layer Flows, Part I: Algorithmic Considerations and Validation," *Theoretical and Computational Fluid Dynamics*, Vol. Vol. 7, pp. 49–76, 1995.

[13] Lele, S. K., "Compact Finite Difference Schemes with Spectral-like Resolution," *Journal of Computational Physics*, Vol. Vol. 103, pp. 16–42, 1992.

[14] Kleiser, L. and Zang, T. A., "Numerical Simulation of Transition in Wall-Bounded Shear Flows," *Ann. Rev. Fluid Mech.*, Vol. Vol. 23, pp. 495–535, 1991.

[15] Zhong, X., "Additive Semi-Implicit Runge-Kutta Schemes for Computing High-Speed Nonequilibrium Reactive Flows," *Journal of Computational Physics*, Vol. Vol. 128, pp. 19-31, 1996.

[16] Zhong, X. and Shen, J. W., "Efficient Semi-Implicit Computations for Unsteady Viscous Hypersonic Flows on Dynamic Grids," *Submitted to Journal of Spacecraft and Rockets*, 1996.

[17] Yoh, J. J. and Zhong, X., "Computations of Multi-Dimensional Detonation Using Semi-Implicit Runge-Kutta Schemes," *AIAA paper 97-0803, 35th AIAA Aerospace Sciences Meeting and Exhibit, January 6-9, Reno, Nevada*, 1997.

[18] Zhong, X., "Direct Numerical Simulation of Hypersonic Boundary-Layer Transition Over Blunt Leading Edges, Part I: New Numerical Methods and Validation ," *AIAA paper 97-0755, 35th AIAA Aerospace Sciences Meeting and Exhibit, January 6-9, Reno, Nevada*, 1997.

[19] Yoh, J. J. and Zhong, X., "Low-Storage Semi-Implicit Runge-Kutta Methods for Reactive Flow Computations," *AIAA paper 98-0130, 36th AIAA Aerospace Sciences Meeting and Exhibit, January 12-15, Reno, Nevada*, 1998.

[20] Zhong, X., "New High-Order Semi-implicit Runge-Kutta Schemes for Computing Transient Nonequilibrium Hypersonic Flow," *AIAA Paper 95-2007*, 1995.

American Institute of Aeronautics and Astronautics

[21] Zhong, X., "Semi-Implicit Runge-Kutta Schemes for Direct Numerical Simulation of Transient High-Speed Reactive Flows," *To appear in the Journal of Computational Physics*, 1996.

[22] Hu, S. H. and Zhong, X., "Linear Stability of Compressible Couette Flow," *AIAA paper 97-0432*, 1997.

[23] Mack, L. M., "Boundary Layer Linear Stability Theory," *AGARD report, No. 709*, 1984.

[24] Zhong, X., "Direct Numerical Simulation of Hypersonic Boundary-Layer Transition Over Blunt Leading Edges, Part II: Receptivity to Sound ," *AIAA paper 97-0756, 35th AIAA Aerospace Sciences Meeting and Exhibit, January 6-9, Reno, Nevada*, 1997.

Table 2: Efficiency comparison between full explicit method and semi-implicit method for the simulations of temporal stability of supersonic Couette flow.

	Full Explicit	Semi-Implicit	Ratio
CFL number	0.0043	0.33	0.013
$\frac{\Delta x}{\Delta y}$	202.95	202.95	–
timesteps	226, 116	3, 000	75.372
time$(sec) \times 10^{-2}$	0.422837	0.422837	–
Record of CPU time(sec) consuming.			
Full Explicit	60, 456.63	–	–
ASIRK-1C	–	3, 518.96	17.1802
LSSIRK-2C	–	7, 144.83	8.4616
LSSIRK-3C	–	11, 541.26	5.2383

Table 3: Efficiency comparison between full explicit method and semi-implicit method for the simulations of temporal stability of supersonic flat plate boundary layer (Time: 2nd order, Space: 5th order).

	Full Explicit	LSSIRK-2C	Ratio
CFL number	0.00284	0.18	–
$\frac{\Delta x}{\Delta y}$	169.2857	169.2857	–
timesteps	126, 702	2, 000	63.351
time$(sec) \times 10^{-2}$	0.1074	0.1074	–
CPU time(sec)	39, 809.77	6, 184.35	6.437

Table 4: Efficiency comparison between full explicit method and semi-implicit method for the simulations of the receptivity of hypersonic boundary layers over blunt body (Time: 2nd order, Space: 5th order).

	Full Explicit	AB-CN	Ratio
CFL number	0.0047	0.14	0.0336
Grids	160×120	160×120	–
$\frac{\Delta x}{\Delta y}$	245.82	245.82	–
timesteps	446, 811	15, 000	29.787
time$(sec) \times 10^{-3}$	1.0091	1.0091	–
CPU time(sec)	213, 037.47	24, 437.55	8.718
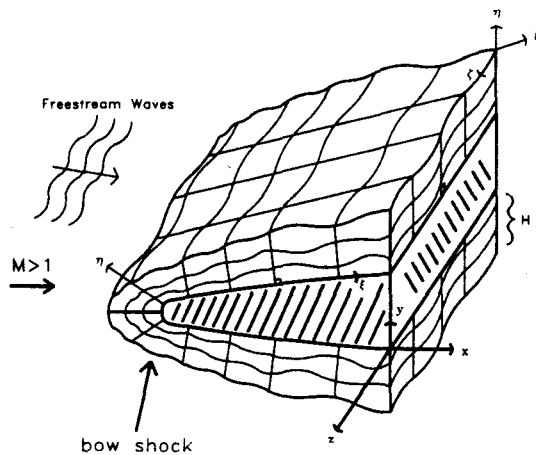
Figure 1: A schematic of 3-D shock fitted grids for the direct numerical simulation of hypersonic boundary-layer receptivity to freestream disturbances over a blunt leading edge.
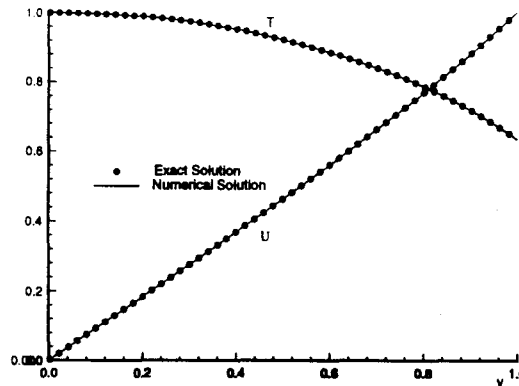
Figure 3: Variation of steady base flow temperature and velocity profiles for adiabatic lower wall with $M_\infty = 2.0$. The numerical solution is obtained using a fifth-order semi-implicit scheme.
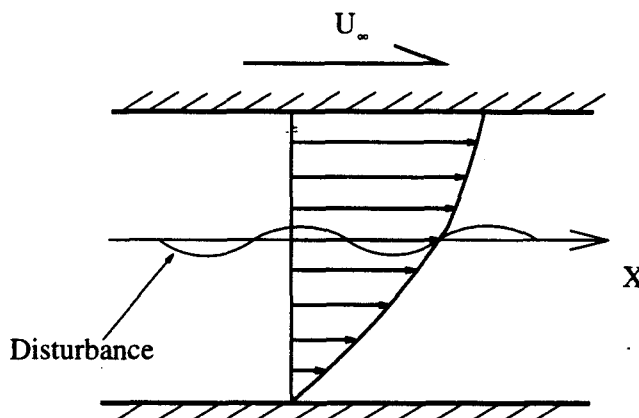
Figure 4: A schematic of stability of two dimensional supersonic Couette flow.
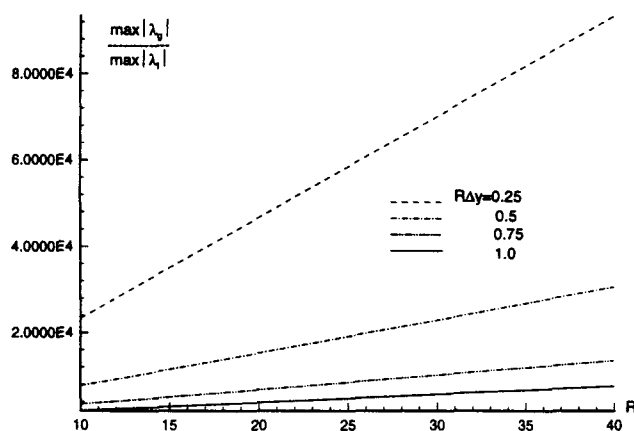
Figure 2: Variation of eigenvalue ratio of maximum eigenvalue of stiff term and maximum eigenvalue of non-stiff term of linearized model equation.
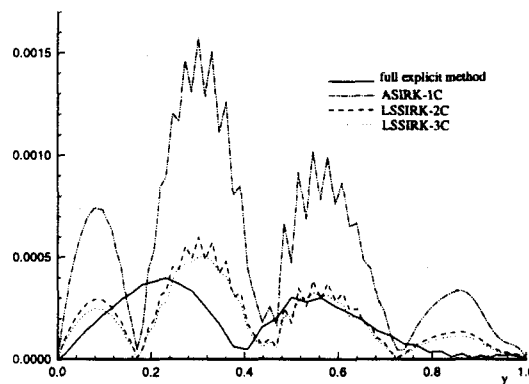
Figure 5: Relative error comparison among full explicit method, ASIRK-1C, LSSIRK-2C and LSSIRK-3C for unsteady Couette flow case with LST results.

American Institute of Aeronautics and Astronautics
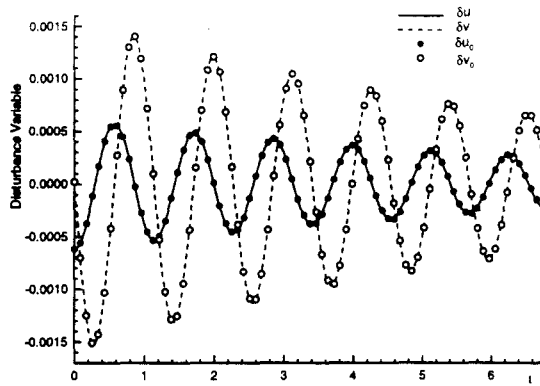
Figure 6: Time history of velocity perturbations at a fixed point in the 2-D supersonic Couette flow field (LST: δu_0 and δv_0, DNS: δu and δv). $M_a = 2.0$, $Re = 1,000$.
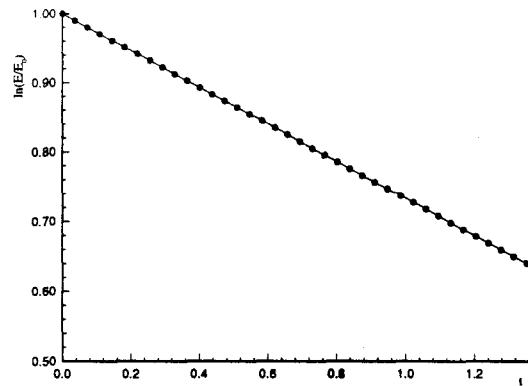
Figure 9: Computed perturbation energy for a 5th-order semi-implicit method. The dot line is the LST result.
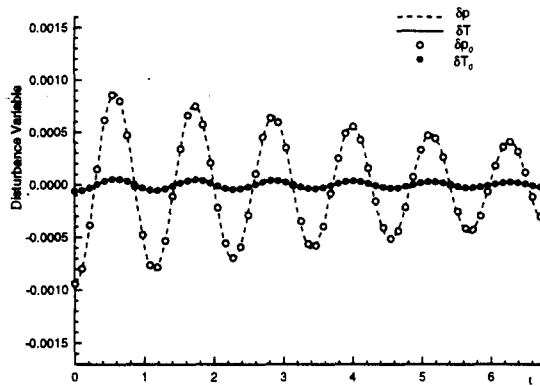
Figure 7: Time history of pressure and temperature perturbations at a fixed point in the 2-D supersonic Couette flow field (LST: δp_0 and δT_0, DNS: δp and δT). $M_a = 2.0$, $Re = 1,000$.
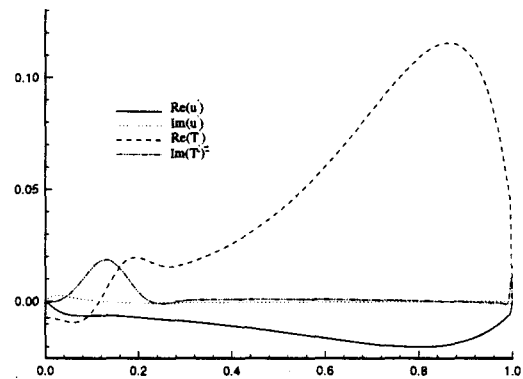
Figure 10: A set of eigenfunctions obtained from linear stability analysis for supersonic Couette flow. $M_a = 5.0$, $Re = 150,000$, $\omega = 0.277395557 + 0.00100708i$.
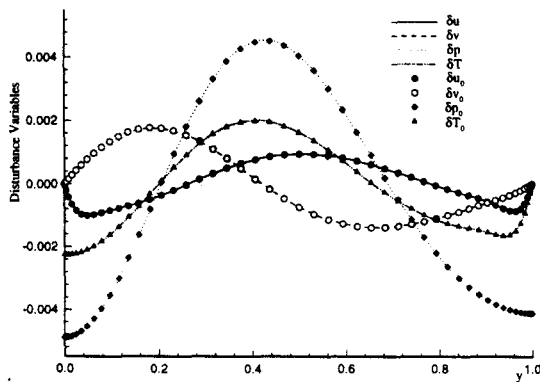
Figure 8: Distribution of instantaneous flow perturbations in y direction. (LST: δu_0, δv_0, δp_0 and δT_0 DNS: δu, δv, δp and δT).
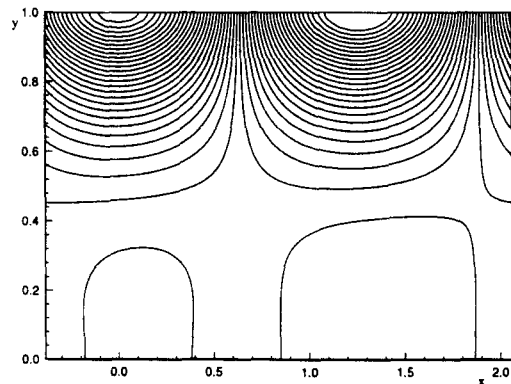
Figure 11: Wave patterns of $Re(p')$ from LST at $M_a = 5.0$, $Re = 150,000$, $\omega = 0.27739555717 + 0.00100708i$.

13

Figure 14: Variation of steady flat plate boundary layer flow velocity profile with $M_\infty = 4.5$, $R = 1,000$. The numerical solution is obtained using a fifth-order semi-implicit scheme.
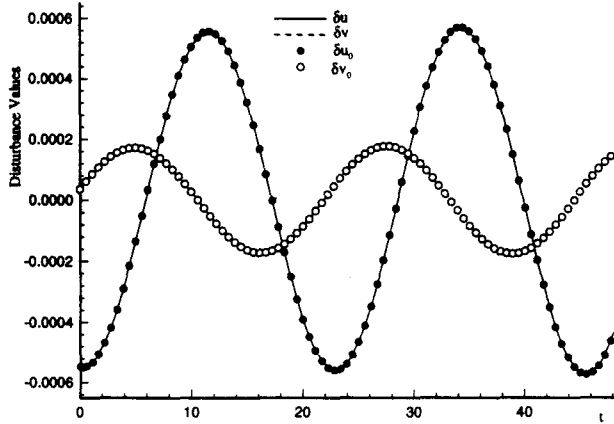

Figure 12: Time history of velocity perturbations at a fixed point in the 2-D supersonic Couette flow field (LST: δu_0 and δv_0, DNS: δu and δv). $M_a = 5.0$, $Re = 150,000$.
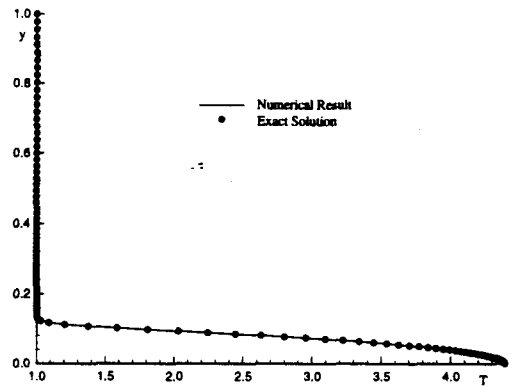
Figure 15: Variation of steady flat plate boundary layer flow temperature profile with $M_\infty = 4.5$, $R = 1,000$. The numerical solution is obtained using a fifth-order semi-implicit scheme.

Figure 13: Time history of pressure and temperature perturbations at a fixed point in the 2-D supersonic Couette flow field (LST: δp_0 and δT_0, DNS: δp and δT). $M_a = 5.0$, $Re = 150,000$.
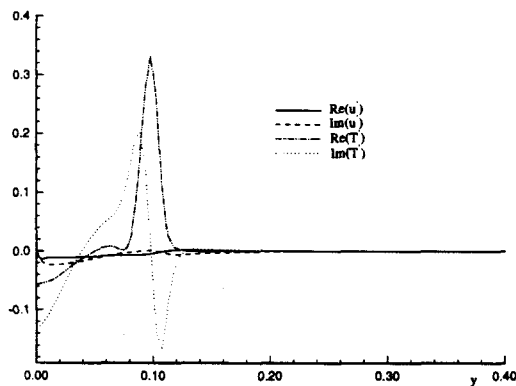
Figure 16: A set of eigenfunctions of unstable second mode obtained from linear stability analysis for supersonic flat plate boundary layer. $M_\infty = 4.5$, $R = 1,000$, $\alpha = 0.22$, $\omega = 25.77363556598 + 0.24971283299918i$.

14
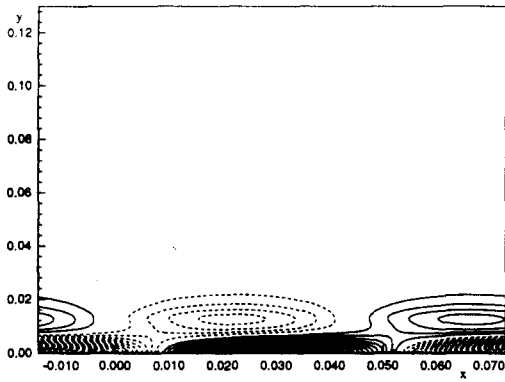
Figure 17: Wave patterns of $Re(p')$ from LST at $M_\infty = 4.5$, $R = 1,000$, $\alpha = 0.22$, $\omega = 25.77363556598 + 0.2497128329918i$.
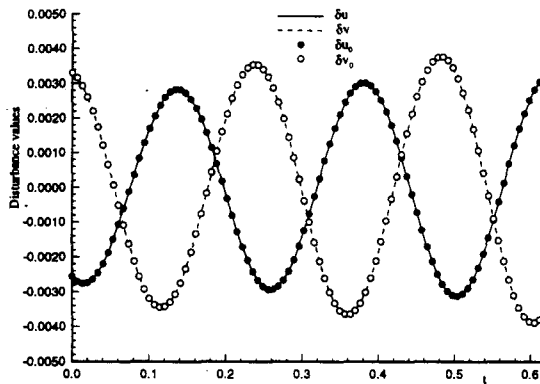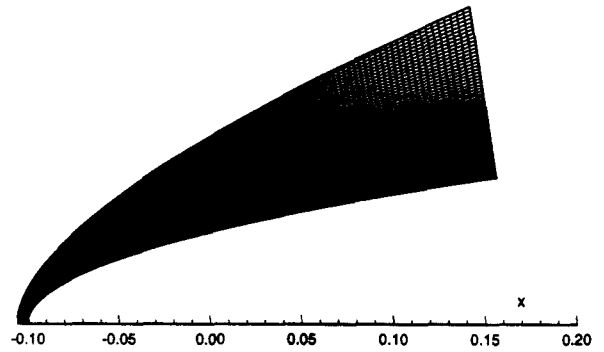
Figure 18: Time history of velocity perturbations at a fixed point in the 2-D supersonic flat plate boundary layer flow field (LST: δu_0 and δv_0, DNS: δu and δv). $M_\infty = 4.5$, $R = 1,000$, $\alpha = 0.22$.
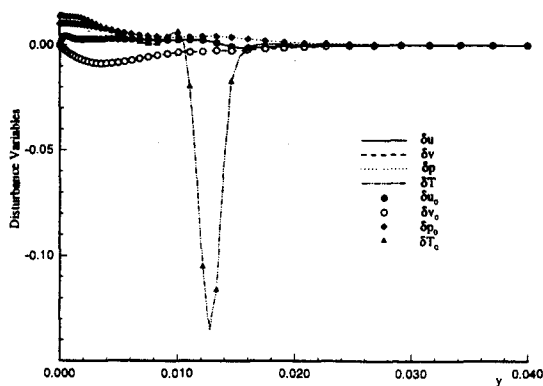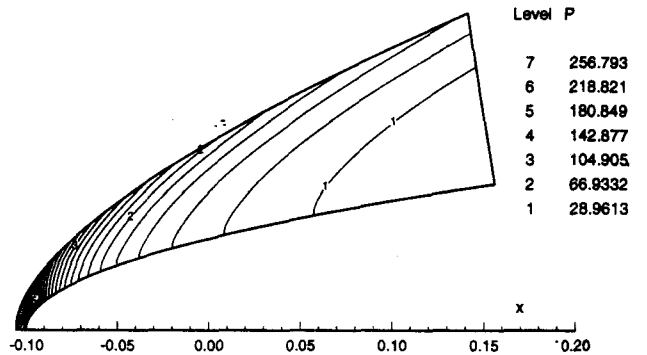
Figure 19: Distribution of instantaneous flow perturbations in y direction. (LST: δu_0, δv_0, δp_0 and δT_0 DNS: δu, δv, δp and δT).
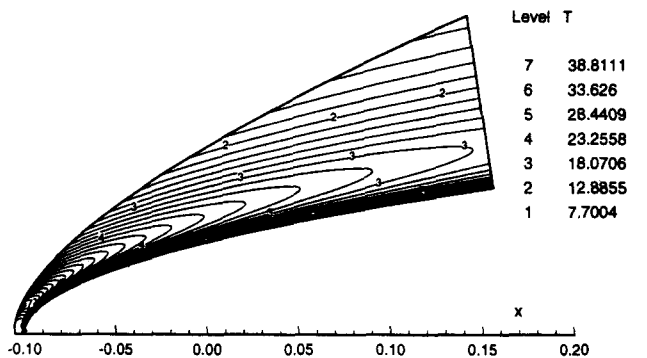
Figure 20: Steady flow solutions by using semi-implicit method for computational grids (upper figure) where the bow shock shape is obtained as the freestream grid line, pressure contours (middle figure), and Temperature contours (lower figure).

15

Level	u'
7	0.00298
6	0.00182
5	0.00066
4	-0.00050
3	-0.00166
2	-0.00283
1	-0.00399

Full explicit method
Semi-implicit method

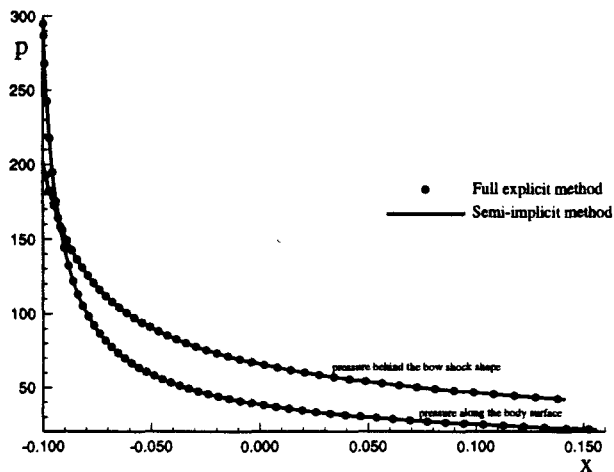pressure behind the bow shock shape

pressure along the body surface

Figure 21: Comparison of steady solution of the pressure profile along the body surface and behind the bow shock shape between full explicit method and semi-implicit method.
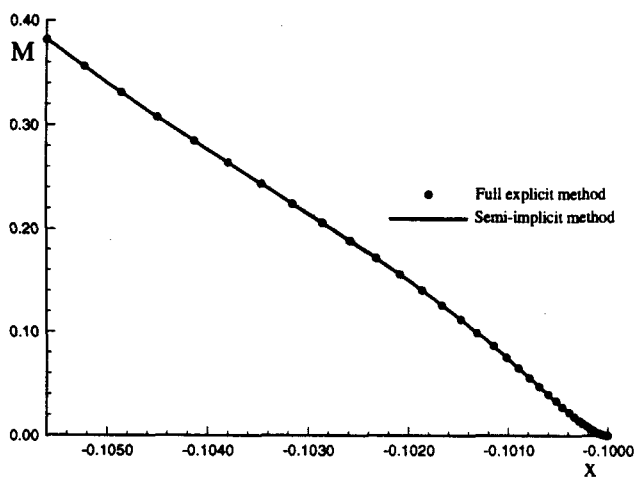
Level	|u'|
8	0.00302
7	0.00261
6	0.00219
5	0.00177
4	0.00136
3	0.00094
2	0.00052
1	0.00010

Level	φ_u
6	303
5	246
4	189
3	133
2	76
1	19

Full explicit method
Semi-implicit method

Figure 23: Unsteady horizontal velocity perturbation contours for the case of $k = 15$: instantaneous u' (upper figure), Fourier amplitude $|\ u'\ |$ (middle figure), and Fourier phase angle $\varphi_{u'}$ (in degrees) of u' (lower figure).

Figure 22: Comparison of steady solution of the Mach number along the stagnation line between full explicit method and semi-implicit method.

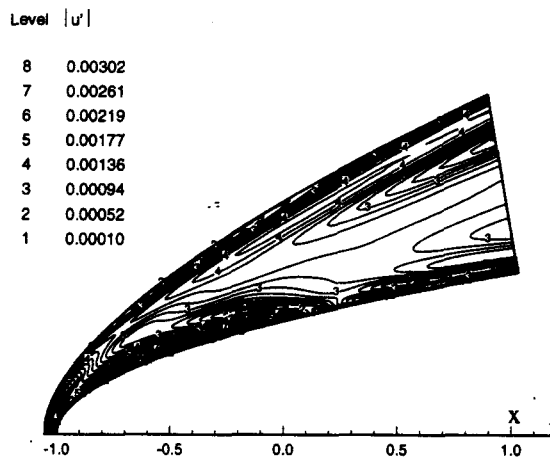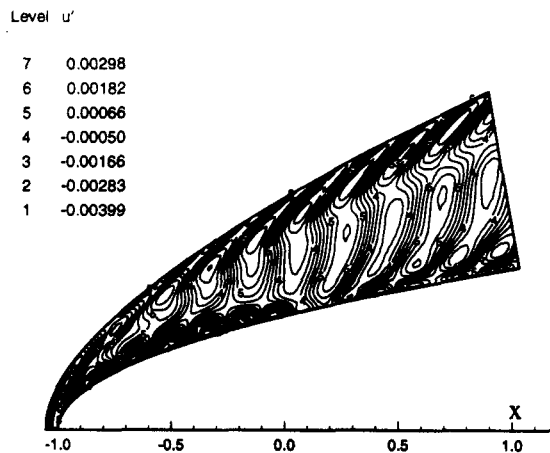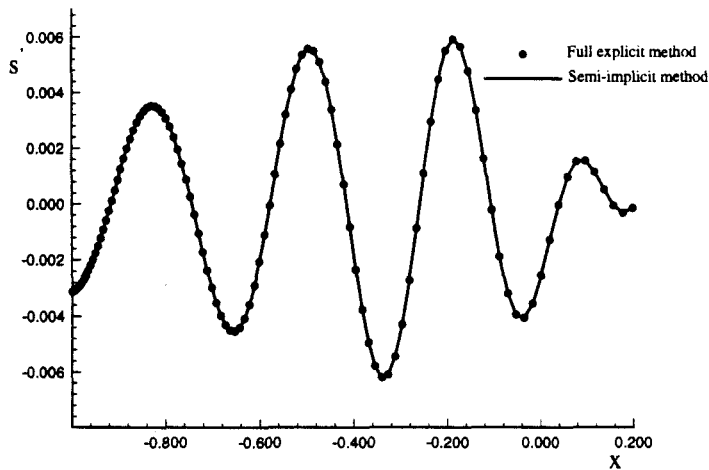American Institute of Aeronautics and Astronautics

Figure 24: Comparison of distribution of instantaneous entropy perturbations along the parabola surface between the full explicit method and semi-implicit method.
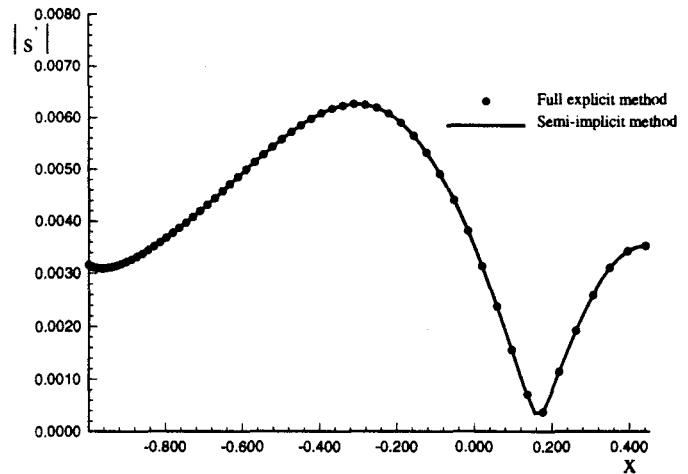

Figure 26: Comparison of distribution of the Fourier amplitudes of the entropy perturbations along the parabola surface between the full explicit method and semi-implicit method.
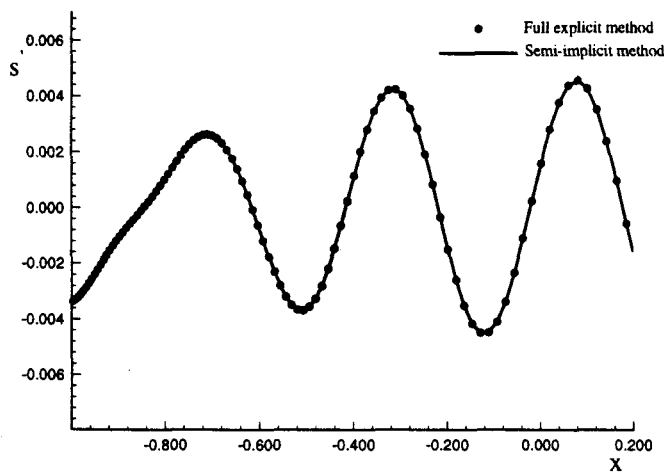

Figure 25: Comparison of distribution of instantaneous entropy perturbations behind the bow shock between the full explicit method and semi-implicit method.
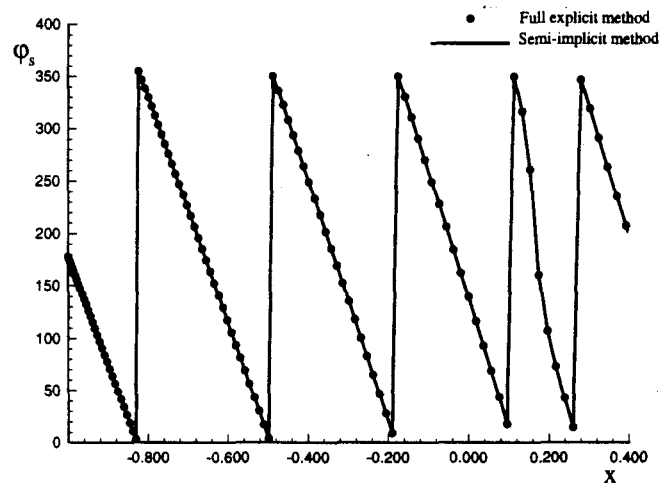

Figure 27: Comparison of distribution of Fourier phase angles (in degrees) of the entropy perturbations along the parabola surface between the full explicit method and semi-implicit method.

17